



The role of intrinsic stacking fault in facilitating the pressure-induced phase transition in CoCrFeMnNi high entropy alloys

Chih-Ming Lin ^{a,*}, Ching-Pao Wang ^b, Sean R. Shieh ^b, Yao-Jen Chang ^c, Tony Huang ^d, Dong-Zhou Zhang ^e, Chin-Wei Wang ^f, An-Chou Yeh ^c, Jenh-Yih Juang ^{g,**}

^a Department of Physics, National Tsing Hua University, Hsinchu, 30013, Taiwan

^b Department of Earth Sciences, University of Western Ontario, London, ON, Canada, N6A 5B7

^c Department of Materials Science and Engineering, National Tsing Hua University, Hsinchu, 30013, Taiwan

^d Department of Earth Sciences, National Cheng Kung University, Tainan, 701, Taiwan

^e GeoSoilEnviroCARS, Argonne National Laboratory, USA

^f National Synchrotron Radiation Research Center, Hsinchu, 300076, Taiwan

^g Department of Electrophysics, National Yang Ming Chiao Tung University, Hsinchu, 30050, Taiwan



HIGHLIGHTS

- For CoCrFeNi HEAs, there was no pressure-induced phase transition observed up to the highest applied pressure of 24 GPa.
- For CoCrFeMnNi HEA, wherein the intrinsic stacking fault (ISF) began to appear at 1.7(1) GPa.
- FCC to HCP structural phase transition was found to emerge at around 7.0(1) GPa in CoCrFeMnNi.
- ISF appears to trigger the *fcc-to-hcp* phase transition at around 7.0(1) GPa.

ARTICLE INFO

Keywords:

High-entropy alloy
Extrinsic stacking fault (ESF)
Intrinsic stacking fault (ISF)
Pressure-induced phase transitions

ABSTRACT

The pressure-induced phase transitions in CoCrFeNi and CoCrFeMnNi high entropy alloys (HEAs) at ambient temperature at pressure up to 24.0(2) and 19.4(2) GPa, respectively, were investigated using angle-dispersive X-ray diffraction (ADXRD). Structurally at ambient pressure, both CoCrFeNi and CoCrFeMnNi HEAs consist of face-centered cubic (*fcc*) structure with different lattice constants which are arisen primarily from the cellular growth of alloy during solidification. *In-situ* ADXRD measurements revealed no evidence of structural transformation in CoCrFeNi HEAs up to 24.0(2) GPa. The intrinsic stacking fault (ISF) begins to appear at 1.7(1) GPa and sustains up to 19.4(2) GPa. Moreover, an *fcc* to hexagonal close-packed (*hcp*) structural phase transition emerges at around 7.0(1) GPa in CoCrFeMnNi HEAs. The pressure dependent lattice constants and volume compression yield the zero-pressure isothermal bulk moduli of 187(4) GPa while the normalized *c/a* ratio 1.636(1) for the resultant *hcp* phase. The quantitative correlation of the ISF diffraction intensity shows that the appearance of ISF disrupts the crystal lattice to trigger, at around 7.0(1) GPa, *fcc-to-hcp* phase transition which persists sluggishly to the highest experiment pressure. Neutron powder diffraction (NPD) at pressure up to 8.9(2) GPa was performed in CoCrFeMnNi HEAs at ambient temperature to clarify the significance of pressure induced suppression of local magnetic moment on destabilization of the initial *fcc* structure. The results, however, suggest that the magnetism may only play a minor role, if not none, in facilitating the pressure-induced *fcc-to-hcp* phase transition in CoCrFeMnNi HEAs.

1. Introduction

As one of the primary thermodynamic parameters, pressure has been

ubiquitously adopted to “modify” the physical properties of a material in rather remarkable fashions. Specifically, pressure-induced structural transitions are commonly applied to manipulate optical, electronic and

* Corresponding author.

** Corresponding author.

E-mail addresses: cm_lin@phys.nthu.edu.tw (C.-M. Lin), jyjuang@g2.nctu.edu.tw (J.-Y. Juang).

magnetic properties. Zhang et al. [1] reported a pressure-induced phase transition in the CoCrFeNi solid-solution alloy from *fcc* to *hcp*, emerging at a pressure ~ 13.5 GPa in the pressure transmitting medium of methanol/ethanol mixture and neon gas. Even more interestingly, the transition was very sluggish and did not complete with an applied pressure up to ~ 40 GPa. As a result, the *hcp*-structured phase can be easily quenched to ambient conditions. Polymorphic transition from *fcc* to *hcp* structure has also been observed in CoCrFeMnNi HEAs at pressure around 22.1 GPa [2]. Nevertheless, the transition was irreversible. It was concluded that [2] the *fcc*-structured phase is a stable polymorph at high temperatures while the *hcp*-structured phase more thermodynamically favorable at lower temperatures. Very recently, Tracy et al. [3] reported the martensitic transformation in CoCrFeMnNi HEAs beginning at around 14 GPa. They attributed such a transformation to the local magnetic moment suppression-induced destabilization of the initial *fcc* structure. The transformation was also found very sluggish and the *fcc* to *hcp* transition persists beyond 40 GPa. Moreover, the behavior of CoCrFeMnNi HEAs is unique in that the *hcp* phase retains even after decompression to ambient pressure. As a result, the resultant system consists of metastable *fcc*-*hcp* mixtures. Iota et al. [4] and Torchio et al. [5] indicated that the magnetism in 3d metals is typically suppressed by the application of external pressure, due to a pressure-induced breakdown of the magnetism. They suggested that the decreasing density of states at the Fermi level by external pressure spreads the *d* bands, thus quenching the magnetic moments of 3d atoms and driving the system towards a nonmagnetic state [4,5]. Alternatively, it is conceived that the high-pressure *fcc*-to-*hcp* transformation can take place by virtue of only small atomic displacements associated with the formation of stacking faults (SF), which facilitates the formation of local *hcp* phase within an *fcc* matrix. However, evidences that directly support the notion of SF formation in inducing the *fcc*-to-*hcp* transition are still lacking. In addition, Niu et al. [6] compared the magnetic configurations of CoCrNi with that of other equiatomic ternary derivatives of CoCrFeMnNi and pointed out that the magnetic and chemical aspects might also play a role in leading to the phase transformation. Specifically, the magnetically frustrated Mn tends to eliminate the energy difference between *fcc* and *hcp* structures. As a result, while CoCrNi could exhibit a *fcc*-*hcp* phase transformation after being tensile deformed to about 55% true strain via dislocation slip and interaction with the internal boundaries, such transformation was absent in the parent quinary CoCrFeMnNi and its other ternary derivatives.

In this work, the pressure-induced phase transitions in CoCrFeNi and CoCrFeMnNi HEAs are systematically investigated in a comparative and quantitative manner by angle dispersive X-ray diffraction (ADXRD) measurements. Using the PeakFit software to deconvolute the obtained XRD patterns, we demonstrate the strong effect of manganese addition on the lattice distortion in CoCrFeNi HEAs. The pressure-suppressed local magnetic moment in CoCrFeMnNi HEAs at ambient temperature were also investigated using neutron powder diffraction (NPD) at pressure up to 8.9(2) GPa. More significantly, to the best of our knowledge, this study is the first to experimentally demonstrate the evidence of pressure-induced formation of intrinsic stacking fault (ISF), which is followed subsequently by the *fcc*-to-*hcp* phase transition in *fcc* CoCrFeMnNi HEAs. The present results, thus, should shed some light on resolving the underlying reasons resulting in the scattered results reported previously.

2. Experiments

2.1. Alloy preparation: synthesis and phase identification

The CoCrFeNi and CoCrFeMnNi HEAs used in the present study were prepared by vacuum-arc melting. A total amount of 50 g pure Co, Cr, Fe, Mn, Ni (with purity higher than 99 wt%) were melted in equal molar ratio for each alloy system under a vacuum of 1.01×10^{-3} Pa after purging with high purity argon for three times. The melting process was

repeated for at least 5 times to ensure chemical homogeneity of the alloy in a water-cooled Cu crucible. The solidified cast was cut into samples for further analyses. Samples obtained from the position near the Cu-side were chosen to avoid heavier segregation and shrinkage defects. In order to confirm the consistence of microstructures of the CoCrFeNi and CoCrFeMnNi HEAs, specimens were observed under JSM-7610F high-resolution thermal field emission scanning electron microscope (HRFEG-SEM) equipped with an electron backscatter diffraction (EBSD) system by Oxford Instruments. The specimens were subjected to standard metallurgical sample preparation protocol and the final polishing was conducted using $0.02\text{ }\mu\text{m}$ silica nanoparticles before the EBSD analysis. Optical micrographs of specimens after being polished and etched were also taken to reveal the solidification structure.

2.2. ADXRD under high pressure

In general, a typical pressure profile in high pressure studies show that the pressure gradient is rather large and the region with the highest pressure is only about $10\text{ }\mu\text{m}$ in diameter. In order to minimize the pressure gradient effects on the measurement results, in this study a small beam size was adopted.

2.2.1. The Kirkpatrick-Baez (KB) focusing system

The focused X-ray beam size ADXRD measurements were performed at pressures up to 24.0 and 19.4 GPa for CoCrFeNi and CoCrFeMnNi HEAs, respectively, at beamline BL13-BMC, Advanced Photon Source (APS). APS BL13-BMC system uses a Kirkpatrick-Baez (KB) geometry focusing system. A focused X-ray beam with size of approximately $26\mu\text{m} \times 28\mu\text{m}$ (*H* \times *V*) can be readily achieved with sufficient intensity to perform diffraction studies. Such a system extends the high-pressure x-ray diffraction studies in two regards. (1) The possibility of achieving an even smaller beam size without much loss in intensity. (2) The resolution offered by this method is several times better than unfocused X-ray beam size method. A diamond pen was used to gently scrape samples with a thickness of about $50\text{ }\mu\text{m}$ from the cast. After scraping, the sample was kept at room temperature for two weeks to release the possible residual stress introduced by the scraping process. The CoCrFeNi and CoCrFeMnNi HEAs samples (around $100\mu\text{m} \times 100\mu\text{m} \times 50\text{ }\mu\text{m}$) were loaded in a membrane-driven symmetric diamond anvil cell (DAC) with a pair of $600\text{-}\mu\text{m}$ culet diamonds. X-rays with wavelength of 0.4339 \AA were used for CoCrFeNi and CoCrFeMnNi HEAs measurements. Diffraction patterns were collected using a Mar-345 online imaging plate (2 each) two-dimensional detector. The geometry of the experimental set-up is depicted schematically in Fig. 1. The parameters need to be determined are: D_0 , the distance from the sample to the Mar-345 online imaging plate measured perpendicular to the imaging plate; Z_0 , the zero point; α , the tilt angle of the imaging plate (*i.e.* the deviation from a direction perpendicular to the incoming beam); and λ , the wavelength. The relation between the measured position of diffraction line and 2θ angle is given by:

$$Z - Z_0 = D_0[\tan(2\theta - \alpha) + \tan(\alpha)] \quad (1)$$

Differentiating Eq. (1), one can obtain the angular resolution or so-called angular step size:

$$\Delta 2\theta(2\theta, \text{rad}) = [\Delta Z \times \cos^2(2\theta - \alpha)] / D_0 \quad (2)$$

where ΔZ is the physical line width of a reflection on the imaging plate. From Fig. 1:

$$\Delta Z = (d_{\text{beam}} + D\Delta\theta) / \cos(2\theta - \alpha) = \{d_{\text{beam}} + [D_0\Delta\theta / \cos(2\theta - \alpha)]\} / \cos(2\theta - \alpha) \quad (3)$$

where d_{beam} is the vertical beam size of the incident X-ray. Replacing the ΔZ in Eq. (2) by Eq. (3), one obtains:

$$\Delta 2\theta(2\theta, \text{rad}) = 2[d_{\text{beam}} \cos(2\theta - \alpha)] / D_0 \quad (4)$$

LaB₆ is used as the standard to calculate the D_0 and α parameters, which are 164.3975 mm

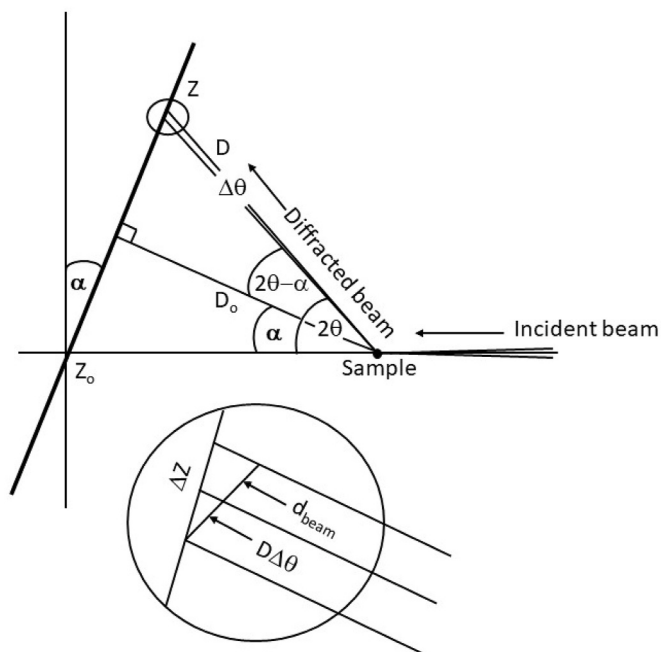


Fig. 1. Schematic representation of the geometry of the experimental setup. D_0 is defined as the perpendicular distance between sample and MAR-345 online imaging plate (2 each). α is a tilt angle of the imaging plate defined as the angle between the imaging beam.

and 0.178549° , respectively. Consideration in choosing the pressure standards is the overlap between the diffraction peaks of the standards and that of the sample. Usually, it is chosen among Au, Pt and MgO, because they all have simple fcc structure and their diffraction peak positions are very close to those of the fcc CoCrFeNi and fcc CoCrFeMnNi HEAs. The 2θ angular resolution for the (111) and (200) diffracting plane of the fcc structure with a wavelength of 0.4339 \AA are 0.0191° and 0.0190° , respectively. Fine ruby spheres [7] were simultaneously distributed around the sample with a pressure-transmitting fluid (PTF)

consisting of Neon gas (as shown in Fig. 2). Klotz et al. [8] reported that the first signs of non-hydrostaticity of Neon appeared at around 15 GPa , which was consistent with the indications given by the R_1 line width and with an earlier work by Meng et al. [9]. Hence, the Neon gas seems to be a suitable PTF for the present high-pressure study. The pressure across the experimental volume is usually inhomogeneous and uniaxial stress and shear stresses might appear. Ensuring the precise pressure readings by uniformly distributing ruby sphere across the bore is very important for our study, which is meant to unveil the effect of Mn and the onset of phase transition. The pressure was increased at a rate of $\sim 0.4 \text{ GPa/min}$ between measurements to avoid abrupt kinetic constraints on phase transformation. The diffraction peaks of ADXRD reported in this study was obtained using Voigt curve fitting.

2.2.2. The collimated focusing system

In order to check the possible effects of the X-ray beam size, additional ADXRD measurements were carried out on the beamline BL01C2 at the National Synchrotron Radiation Research Center (NSRRC), Taiwan. The wavelength of the collimated X-ray of BL01C2 was 0.43504 \AA (28.5 keV) with a beam size of $\sim 150 \mu\text{m}$ in diameter. The initial thickness of the 301 stainless steel gasket was $250 \mu\text{m}$, which was then pre-indented to a thickness of about $70\text{--}80 \mu\text{m}$. A sample chamber of about $235 \mu\text{m}$ in diameter was drilled at the center of the indented gasket using a discharge machine. The obtained CoCrFeMnNi HEAs sample was loaded into the sample chamber until the entire sample chamber is filled. Fine ($\sim 1\text{--}2 \mu\text{m}$) ruby powders were simultaneously placed inside the sample chamber with a PTM consisting of a mixture of methanol and ethanol with a ratio (in volume) of 4:1 (methanol/ethanol) [8]. The CoCrFeMnNi HEAs sample was placed on top of the ruby powders and the ruby fluorescence spectra were measured at the same spot.

2.3. Neutron powder diffraction (NPD) measurements under ambient and high pressure

The *in-situ* pressure dependent neutron powder diffraction (NPD) experiments were conducted at ambient temperature on the high-intensity diffraction beamline (Wombat) at the Australian Nuclear Science and Technology Organization (ANSTO) [10]. The Wombat powder diffractometer is located on the TG1 thermal guide at the OPAL reactor. The neutron wavelength of $\lambda \sim 1.5415 \text{ \AA}$ from the vertically focusing Ge 115 monochromator at a 90° takeoff angle was selected for this work. The wavelength was calibrated using the NIST SRM 660b. Wombat possesses a curved two-dimensional (2D) position sensitive detector (PSD) covering an angular range of 120° and with a high-speed readout capability (up to 10^6 cps). Therefore, the NPD experiments for small-size samples are feasible on Wombat. The VX-5 type Paris-Edinburgh (P-E) press with the tungsten carbide (WC) anvils was used in the present work. A hydraulic pump is attached to the P-E cell, allowing pump up the pressure manually. The lead (Pb) fragments were chosen as the internal pressure gauge. The deuterated 4:1 methanol-ethanol was used as the pressure-transmitting medium (PTM) in the present NPD experiment. We used the “rasp-powdered sample” prepared from the ingot to prevent the collected NPD patterns from the preferred orientation effects commonly encountered in CoCrFeMnNi ingots. Together with the lead pressure gauge and the PTM, the powder sample was loaded into the encapsulated gasket made of the TiZr null-matrix alloy. The collected diffraction patterns were analyzed using the Fullprof suite [11]. The whole pattern fitting including both diffraction peaks from the HEAs and lead enables accurate determination of the pressure dependence of lattice constant.

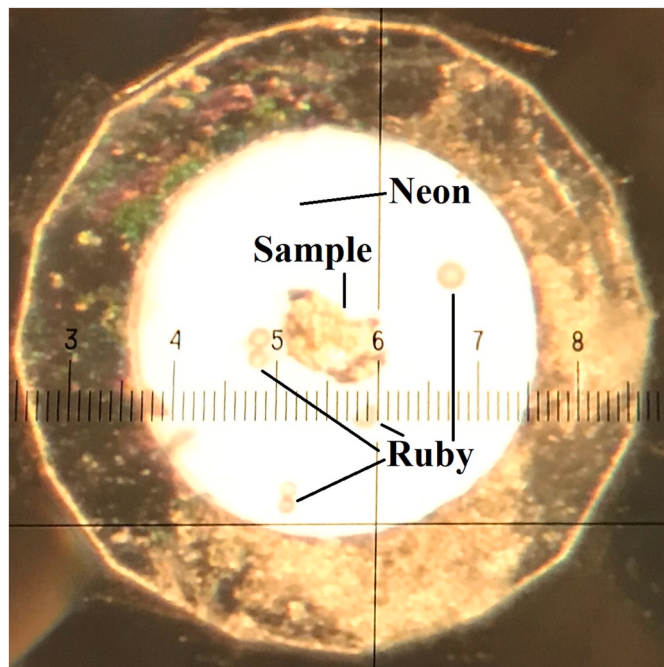


Fig. 2. Ruby spheres are simultaneously approximate average distributed around the sample with a Neon pressure-transmitting fluid.

3. Results

3.1. Structural characteristics of CoCrFeNi HEAs under ambient pressure by ADXRD

Fig. 3(a) shows the representative *in-situ* ADXRD spectrum of CoCrFeNi HEAs obtained at ambient condition and that of the cubic Ni with $Fm\bar{3}m$ space group ($a = 3.499 \text{ \AA}$). The ADXRD pattern of CoCrFeNi HEAs at ambient pressure shows that the structure is essentially single-phased *fcc*. Nonetheless, the shape of the (111) and (200) diffraction peaks suggests that the seemingly *fcc*-structured matrix might consist of multiple distinguishable structures [12]. As has been pointed out by Balogh et al. [13], by using X-ray line profile analysis, it is possible to delineate the density of planar defects along with the associated dislocations in *fcc* crystals. In **Fig. 3(a)**, a discernible new diffraction peak at 2θ (Bragg angle) $\approx 11.4961^\circ$ (indicated by the green dash arrow) manifested as a shoulder on the left-hand side of the (111) diffraction peak of the *fcc*-structured CoCrFeNi HEAs can be resolved, as shown in the inset. This feature signifies the existence of extrinsic stacking fault (ESF) in CoCrFeNi HEAs [14]. Wang et al. [14] pointed out that the quaternary CoCrFeNi HEAs had a much higher tendency to form ESFs, which, in turn, resulted in severe lattice distortion and the asymmetric profile of the (111) diffraction peak. Since for ESF, an extra plane is inserted into the stacking sequence of the (111) planes, resulting in severe local lattice distortion and asymmetric effect, thus it is plausible to expect a satellite peak albeit with much weaker intensity might appear adjacent to the (111) diffraction peak, as illustrated in **Fig. 3(a)**. In addition, Warren et al. [15] indicated that, due to the existence of ESF, the (111) reflection would move toward a larger diffraction angle while the (200) reflection shifts oppositely toward a smaller diffraction angle. Namely, the separation of these two peaks would decrease as a result of stacking faults. Warren [16] further reported that the change in peak separation of the (111)–(200) pair due to deformation faulting can be described by the following expression:

$$\Delta(2\theta_{200} - 2\theta_{111})^\circ = \frac{-90\sqrt{3}\alpha_{df}}{\pi^2} \left(\frac{\tan \theta_{200}}{2} + \frac{\tan \theta_{111}}{4} \right) \quad (5)$$

Wherein, the parameter α_{df} can be regarded as the probability of finding a deformation fault between any two layers. Consequently, parameter $1/\alpha_{df}$ reflects the average number of layers between two faults. **Fig. 3(b)** shows the measured separations $2\theta_{200} - 2\theta_{111}$ for the as-cast CoCrFeNi HEAs and that of the cubic Ni with $Fm\bar{3}m$ space group, which is assumed to have no fault. Within the context of the Warren's model, the decrease of $\delta(2\theta_{200} - 2\theta_{111})^\circ$ can account for the amount of deformation faulting produced during the casting process. The results shown in **Fig. 3(b)**, thus, give $\Delta(2\theta_{200} - 2\theta_{111})^\circ = -1.382 \alpha_{df}$. The obtained $\alpha_{df} = -0.032/(-1.382) = 0.023$, then gives $1/\alpha_{df} \approx 43$, implying that, on the average, there is one stacking fault for approximately every 43 (111)-stacking layers existing in the as-cast CoCrFeNi HEAs. The number is, in fact, very close to that observed in cold-worked alpha Brass [15] and is consistent with the highly distorted nature of HEAs. The intensity of hkl reflections in XRD pattern is often regarded as directly proportional to the concentration or the volume fraction of the corresponding phase component [17]. Thus, although the fraction of 0.023 is small, it might be still marginally detectable in XRD. We estimate the intensity for a series of N crystal planes of an ESF with a distance D_0 apart from a perfect crystal following the analyses proposed by Fewster et al. [18], namely, $I \propto \left| \frac{\sin \left\{ N \left[\frac{\pi d}{\lambda} (2\sin \theta_B) - n\pi \right] \right\}}{\sin \left[\frac{\pi d}{\lambda} (2\sin \theta_B) - n\pi \right]} \right|^2$. The estimated relative

ratio between the ESF and *fcc*(111) peak intensity is approximately 0.0056, which is in reasonable agreement with what is seen in **Fig. 3(a)**. Moreover, **Fig. 3(a)** shows that the *d*-spacing of *fcc*(111) and ESF are 2.0610(1) and 2.1667(1) \AA , respectively, indicating that the ESF

produced by interstitial agglomeration of faulted layers may have induced an expansion of *fcc*(111) *d*-spacing by about 5%. It is not clear at present exactly what causes the formation of ESFs in the quaternary CoCrFeNi HEAs during the casting process. Nevertheless, mechanisms, such as the mixed effects of magnetic fluctuations [19] and severe lattice distortion resulting from the atomic radius difference of the constituent elements, have been conceived to be possible reasons as both are capable of offering the necessary space for one extra (111) plane to be inserted in the *fcc* lattice and result in formation of ESFs.

In order to further clarify that the observed results are not originated from inhomogeneities, the present quaternary CoCrFeNi HEAs were further examined by SEM-EBSD to delineate their solidification structure and composition distributions. **Fig. 4** shows the typical inverse pole figure (IPF) obtained by SEM-EBSD (**Fig. 4(a)**) together with an optical image (**Fig. 4(b)**). In **Fig. 4(a)**, the Ni-*fcc* phase was chosen for phase acquisition and the entire area has been identified as *fcc* phase in IPF image. Thus, the possibility of forming two distinct *fcc*-like phases can be excluded. In **Fig. 4(b)**, an apparent cellular grain structure is evident. The composition analysis on the cellular grain core and cell boundary has been conducted by SEM energy dispersive spectroscopy (SEM-EDS) and the results are listed in **Table 1**. It is evident from **Table 1** that cell boundary is relatively rich in Cr, presumably due to the solidification segregation effects. Since the atomic radius of Co, Cr, Fe and Ni are 1.25, 1.28, 1.27 and 1.25 \AA , respectively [20], the lattice constant is expected to expand slightly in the Cr-rich region as compared to that of the designed equiatomic stoichiometry alloy.

3.2. Effects of applied external pressure (P) on the structure of CoCrFeNi HEAs by ADXRD

Fig. 5(a) shows the representative pressure-dependent *in-situ* ADXRD spectra of CoCrFeNi HEAs obtained at room temperature with pressures up to 24.0(2) GPa. In contrast to previous pressure study by Zhang et al. [1], our results show no evidence of *fcc*-to-*hcp* phase transition and the structure remains essentially single-phased *fcc* without any major structural modifications in CoCrFeNi HEAs. It appears that the existence of ESF does not play any role in facilitating the pressure-induced transition in the present quaternary HEAs. However, the peaks did shift (including the ESF satellite peak) with the increasing pressure. As indicated by the green dashed line, the red-shift (to higher angle) of the ESF peak indicates that the interplanar distance of the ESF decreases gradually with increasing pressure. Interestingly, as displayed in **Fig. 5(b)** and **(c)**, the separation between the (111) and (200) peak, $2\theta_{200} - 2\theta_{111}$, exhibits somewhat unusual pressure dependence. Below 10 GPa (**Fig. 5(b)**), the value of $2\theta_{200} - 2\theta_{111}$ (in degree) seems to fluctuate substantially. However, over a wider range of applied pressure (**Fig. 5(c)**), the trend becomes clearer. Namely, in general, the peak separation reduces as a function of increased external pressure, presumably due to the increase of deformation faulting induced by the increased amount of external work. A first order linear fit of **Fig. 5(c)** indicates that the angle of $2\theta_{200} - 2\theta_{111}$ separation, $\Delta(2\theta_{200} - 2\theta_{111})^\circ$, can be approximately expressed as: $\Delta(2\theta_{200} - 2\theta_{111})^\circ = -1.3974 \alpha_{df}$, giving rise to $\alpha_{df} \approx -0.3713/(-1.3974) = 0.2657$ at an external pressure of 24.0(2) GPa. The value of $1/\alpha_{df} \approx 4$ suggests that there will be about one stacking fault for every 4 layers along the (111)-stacking [15,16]. It is interesting to note that, even with such high density of deformation faulting, no apparent effect of pressure on triggering the formation of *hcp* structure was observed in the present CoCrFeNi HEAs sample. It may be that the kinetic barrier for *fcc*-to-*hcp* transition is too high [2], such that the work done exerted by P is not adequate to trigger the structural phase transition but instead appears as the effect of increasing the density of deformation stacking faults.

Volumetric compressibility defines the volume change in a material under P , whilst linear compressibility describes the change along a specified axis of the material. As such, any discontinuity in either compressibility may reflect a structural change in the system. **Fig. 6**

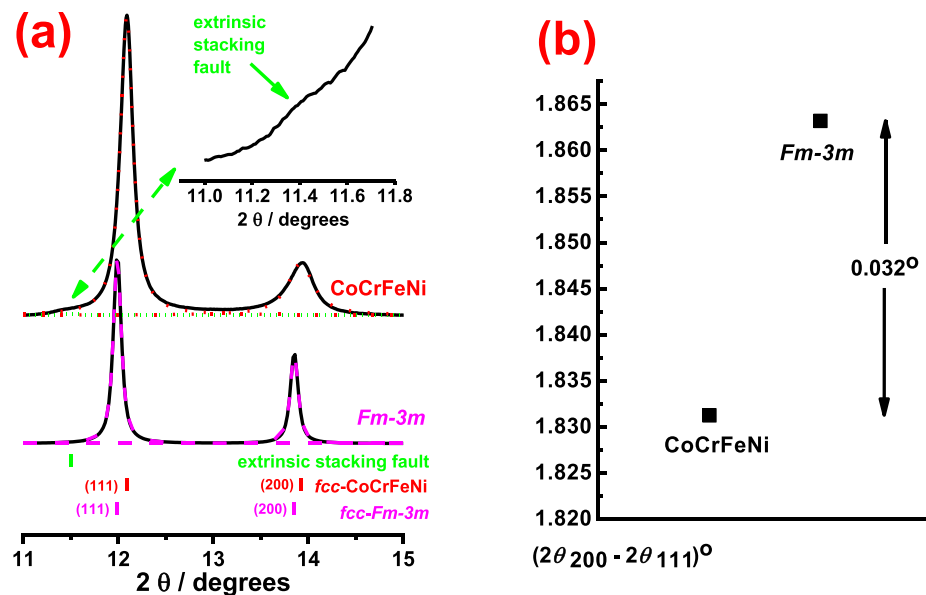


Fig. 3. (a) Representative ADXRD patterns of CoCrFeNi at ambient pressure. (b) Peak separations (111)–(200) for the CoCrFeNi HEAs and cubic $Fm\bar{3}m$ space group.

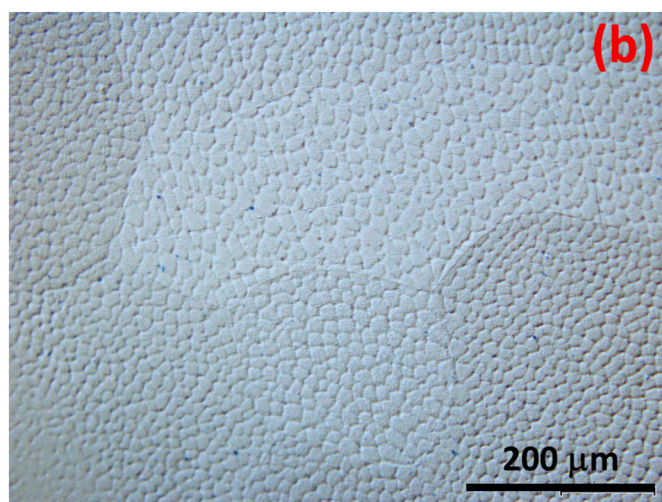
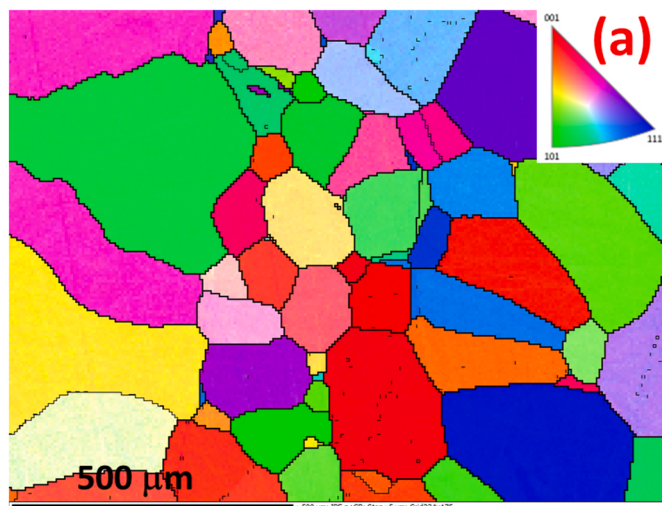


Fig. 4. (a) SEM EBSD IPF image and (b) OM image of microstructure of CoCrFeNi alloy.

Table 1

The composition (in at%) of cell core and cell boundary in CoCrFeNi and CoCrFeMnNi HEAs measured by SEM EDS.

Element	Co	Cr	Fe	Mn	Ni
CoCrFeNi	25.2	25.0	25.7	–	24.0
	23.9	27.2	24.6	–	24.4
CoCrFeMnNi	20.3	21.1	20.5	18.7	19.4
	13.8	13.8	12.0	32.4	28.1

shows the pressure dependence of lattice parameters (a) and unit cell volume (V) of the respective phases. Both the a and V tend to decrease with increasing P . In particular, when P exceeds 20 GPa, the standard deviation of both a and V increases enormously, presumably due to the severe lattice deformation at higher P , which significantly broadens the (200) peak and makes it more difficult to locate the peak position. From Fig. 6(a), the value of the linear compressibility (K_a) is estimated to be $\sim 1.286 \times 10^{-3}$ GPa $^{-1}$, which remains unchanged up to 24.0(2) GPa, suggesting that no structural change occurs over the entire pressure range. Fig. 6(b) shows that a similar trend can be observed for the volume compressibility (K_V). It is interesting to note that the value of $K_V \sim 3.845 \times 10^{-3}$ GPa $^{-1}$ is about 2.99 times of K_a , indicating that the present CoCrFeNi HEAs sample is indeed intrinsically isotropic. The pressure-volume relationship and the bulk modulus data are the essential physical parameters required for establishing the equation of state and characterizing the anharmonic dynamic properties of the system under the effects of pressure. The data when fitted to a second-order Birch-Murnaghan equation of state [21] yield a zero-pressure isothermal bulk modulus (B_0) of 323(5) GPa. This value is about twice larger than that the values of 150.2 ± 4.6 GPa and $141(8)$ GPa for CoCrFeMnNi HEAs reported by Zhang et al. [2] and Tracy et al. [3], respectively, suggesting that the CoCrFeNi HEAs sample is significantly more resistant to compression and might explain the absence of pressure-induced fcc-to-hcp structural transition.

3.3. Structural and magnetic properties of the quinary CoCrFeMnNi HEAs under ambient pressure by NPD

To investigate the temperature dependence of the unit cell parameters and magnetic properties of the quinary HEAs, NPD measurements

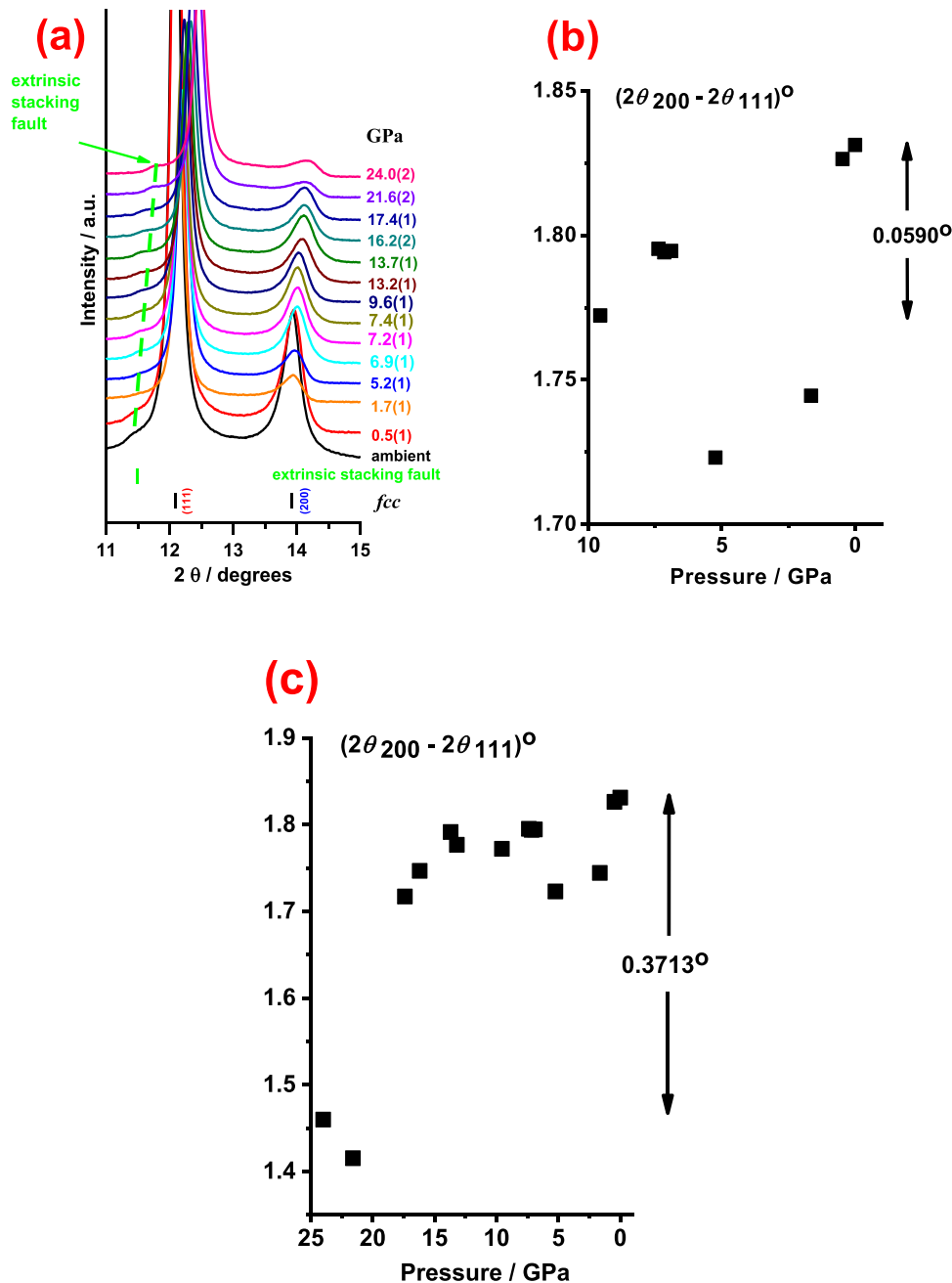


Fig. 5. (a) Representative ADXRD patterns of CoCrFeNi at elevated pressures. (b) Peak separations $2\theta_{200} - 2\theta_{111}$ for the CoCrFeNi HEAs at various applied external pressure.

were performed. Fig. 7(a) shows the temperature dependence of the NPD diffraction patterns obtained between 5 K and 300 K at ambient pressure. From the NPD results, it appears there is no evidence of either structural or magnetic phase transition within the temperature range studied. These observations strongly suggest that the magnetic moments of the alloying elements probably do not play a significant role in destabilizing the fcc structure.

The temperature-dependent lattice parameter obtained from the NPD measurements is shown in Fig. 7(b), from 5 to 300 K. The lattice constants are derived from the (111), (200), (220), (311), (222), and (400) peaks of the fcc phase. The lattice constants at 5 and 300 K are calculated to be 3.5951(1) and 3.6062(1) Å, respectively. The lattice constant at 300 K obtained by NPD is about the same as that (3.5907(2) Å) obtained by ADXRD method for the quinary HEAs (*see below*). The

temperature dependence of the obtained lattice constant can be well described by an empirical formula in exponential form [22]:

$$\frac{\delta L}{L_0} = \frac{L - L_0}{L_0} = \alpha_{HT} T + \alpha_{HT} \Theta_D (e^{-T/\Theta_D} - 1) \quad (6)$$

where L and L_0 are the lattice constants at temperature T and 0 K, respectively; T is the temperature, Θ_D is the Debye temperature, α_{HT} is the value of the coefficient of thermal expansion α in the high temperature limit. Rewrite Equation (6) as follows

$$L = L_0 + L_0 \alpha_{HT} T + L_0 \alpha_{HT} \Theta_D [e^{(-T/\Theta_D)} - 1] \quad (7)$$

The temperature dependence of L of our quinary HEA is shown in black hollow squares in Fig. 7(b). Using $L_0 = 3.5951(1)$ Å, $\alpha_{HT} = 2.8 \times$

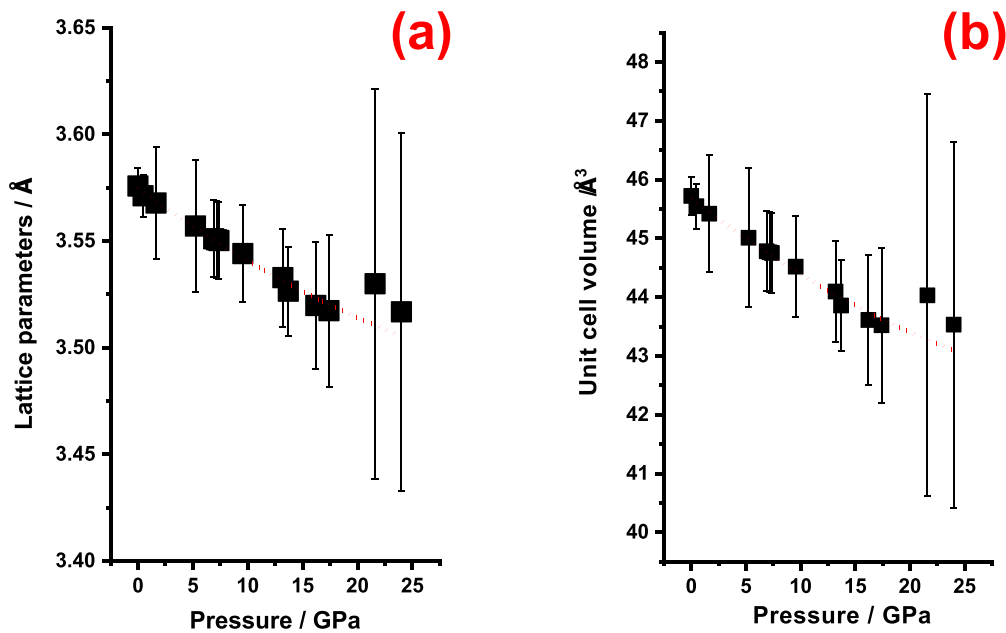


Fig. 6. (a) Pressure dependence of the a of CoCrFeNi at 300 K. (b) Pressure dependence of the unit cell volume of CoCrFeNi at 300 K. The short dotted lines illustrate the results of fitting of a third-order Birch-Murnaghan equation of state to the data corresponding to fcc phase.

10^{-5} K $^{-1}$ and $\Theta_D = 299$ K, an excellent fit is obtained between Equation (7) and the experimental data. Fig. 7(b) clearly shows that lattice constant is not linearly dependent on the temperature over the investigated temperature range from 5 to 300 K. This behavior is similar to that observed previously by Laplanche et al. [23], wherein no phase transformation occurs in the investigated temperature range from 300 to 1270 K. The value of α as a function of temperature is shown in Fig. 7(c), which is obtained by differentiating Eq. (6) to get the following expression:

$$\alpha = \frac{d}{dT} \left(\frac{\delta L}{L_0} \right) = \alpha_{HT} (1 - e^{-T/\Theta_D}) \quad (8)$$

Using Eq. (8), it has been demonstrated that the temperature dependence of α for the quinary HEA behaves similarly to that of conventional fcc steels in the temperature range of 300–1270 K, with α increasing gradually from α (300 K) $\approx 15 \times 10^{-6}$ (K $^{-1}$) to $\alpha_{HT} \approx 24 \times 10^{-6}$ (K $^{-1}$) for T > 1200 K [23]. It is noted, however, the temperature dependence of α for the quinary HEA below 300 K was not explored previously. In our case here, it is evident that the temperature dependence of α for the quinary HEA within 5–300 K has a much stronger temperature dependence. The reason for this is not clear at present, although it appears to follow the similar decreasing trend and the obtained α (300 K) $\approx 17 \times 10^{-6}$ (K $^{-1}$) is also in reasonable agreement with that ($\approx 15 \times 10^{-6}$ K $^{-1}$) reported in [23].

3.4. Effects of P on the structure of the quinary CoCrFeMnNi HEAs

3.4.1. Results from the Kirkpatrick-Baez (KB) focusing system

Fig. 8(a) shows the representative *in-situ* ADXRD spectrum of the quinary HEAs obtained at ambient condition and that of the cubic $Fm\bar{3}m$ space group. The ADXRD pattern of the quinary HEAs at ambient pressure shows that the structure is essentially single-phased fcc. The inter-planar spacings, d -spacings, of the (111) and (200) planes under ambient pressure are 2.0713 and 1.7969 Å, respectively, which appears to be slightly smaller than that of the $Fm\bar{3}m$ space group. Moreover, it is noted that at ambient condition the (111) and (200) diffraction peaks are rather symmetric with no discernible satellites albeit are more

broadened. The unit-cell parameters at ambient pressure determined from the data are $a = 3.5907(43)$ Å, $V/Z = 11.574(42)$ Å 3 ($Z = 4$), respectively. These values are slightly larger than that of CoCrFeNi HEAs sample, where $a = 3.5758(86)$ Å and $V/Z = 11.431(82)$ Å 3 ($Z = 4$), respectively. Apparently, the addition of manganese causes a slight increase in the lattice constant and unit cell volume. In addition, the standard deviation of the lattice constant and unit cell volume of CoCrFeNi HEAs sample is larger than that of the quinary HEAs, indicating that the present quinary HEAs might have a less distorted lattice in as-cast state. Fig. 8(b) shows the measured $2\theta_{200} - 2\theta_{111}$ for the quinary HEAs and cubic $Fm\bar{3}m$ space group, which shows that a change in peak separation of $\Delta(2\theta_{200} - 2\theta_{111})^\circ = -1.3767 \alpha_{df}$ and $\alpha_{df} \approx -0.0177/(-1.3767) \approx 0.0128$. Since the value $1/\alpha_{df} \approx 78$ may be translated into a stacking fault on the average of every 78 layers in the (111)-stackings [15,16]. Comparing with $1/\alpha_{df} \approx 43$ for the CoCrFeNi HEAs in the as-cast state, this implies that the quinary HEAs apparently are having about two times less grown-in stacking faults during the casting processes, which is also consistent with absence of asymmetric diffraction profile and satellites shown in Fig. 8(a). Fig. 9 shows that the quinary CoCrFeMnNi HEAs also have apparent cellular grain structure, albeit the apparently more porosity as compared to that of the quaternary CoCrFeNi HEAs. Moreover, in contrast to the quaternary CoCrFeNi sample, the SEM-EDS analyses of the quinary HEAs show that the cell boundary regions are rich in Mn, as indicated in Table 1. Since Mn has the lowest melting point, thus last to solidify, among the five constituent elements and an atomic radius of 1.26 Å [20], it is reasonable to expect that it would result in Mn-rich cell boundary regions.

To further elucidate how the manganese addition affects the phase stability beyond ambient conditions, detailed pressure-dependent *in-situ* ADXRD measurements were carried out at room temperature. Representative results are displayed in Fig. 10 with P up to 19.4(2) GPa. From the *in-situ* ADXRD spectra shown in Fig. 10 (a), it is noticed that as the pressure reaches 0.9(1) GPa, the intensity of fcc (111) reflection increases at the expense of that of the (200) reflection, indicating that the P results in significant effects on relative stability of respective fcc phases. Moreover, at 1.7(1) GPa, a discernible new satellite diffraction peak starts to emerge adjacent to the right-hand side of the (111) diffraction peak (the green dotted profile in Fig. 10(a)). This feature has

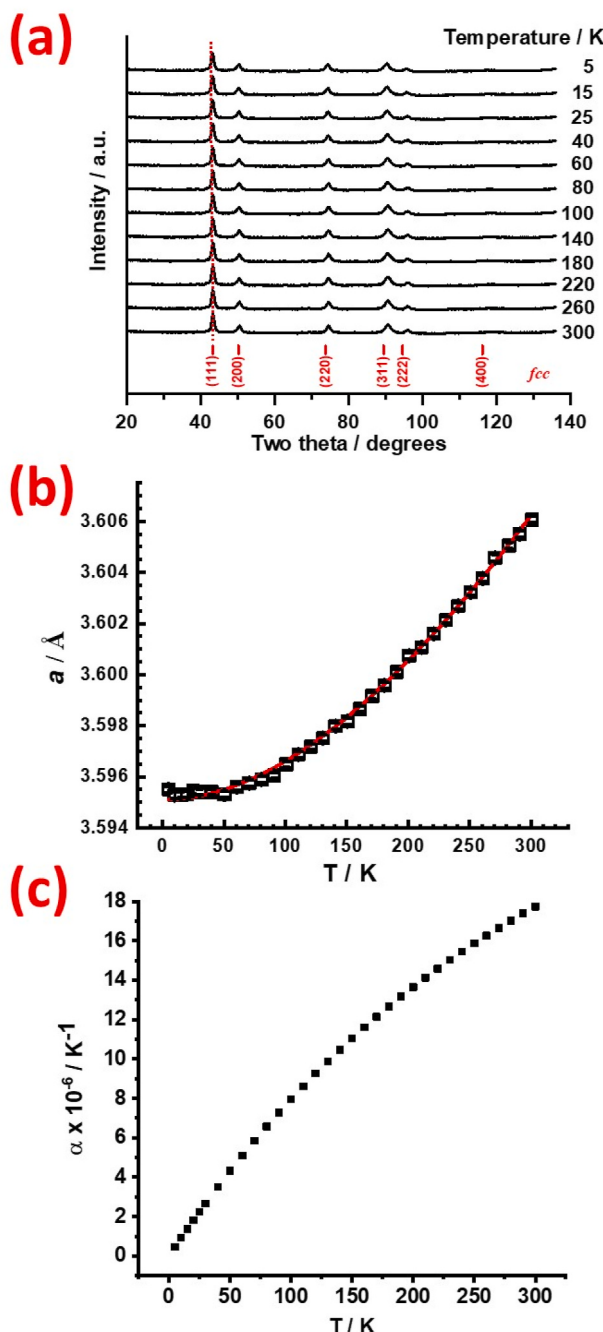


Fig. 7. (a) Neutron powder diffraction (NPD) patterns of CoCrFeMnNi HEAs from 5 K to room temperature. (b) Relative change in a of the CoCrFeMnNi HEAs with temperature. (c) Coefficient of thermal expansion α as a function of temperature for the CoCrFeMnNi HEAs.

been recognized as a manifestation of the existence of regions containing intrinsic stacking fault (ISF) [13]. Fig. 10(c) shows the measured separations $2\theta_{200} - 2\theta_{111}$ for the quinary HEAs at 1.7(1) GPa together with that for the ambient condition. Following the similar analyses based on Warren's model [15,16], the results give rise to $\Delta(2\theta_{200} - 2\theta_{111})^\circ \approx -1.3759 \alpha_{df}$, $\alpha_{df} \approx -0.0267/(-1.3759) \approx 0.0194$ and $1/\alpha_{df} \approx 52$, respectively, and hence indicate that an external pressure of about 1.7 GPa might have increased the density of stacking faults to a similar level ($1/\alpha_{df} \approx 43$) of that generated in the as-cast quaternary CoCrFeNi HEAs. It is obvious that a small work done ($P\Delta V$) has greatly increase the probability of forming deformation stacking faults in the quinary CoCrFeMnNi HEAs. Nevertheless, it should be pointed out that in

quinary CoCrFeMnNi HEAs the primary deformation faulting is ISF [13] unlike that observed in quaternary CoCrFeNi HEAs, wherein the pressure-induced deformation faulting was mainly ESF [14]. It is also evident from Fig. 10(a) that the intensity of ISF satellite peak continues to increase smoothly with increasing applied pressure, while that of the corresponding *fcc* phase behaves in an opposite trend. This indicates that the pressure-induced ISFs are formed via nucleation and growth mechanism within the *fcc* phase. We shall come back to this point later.

As the pressure is further increased to 7.0(1) GPa, the intensity of the ISF peak reaches a maximum value accompanied by a substantial decrease in the intensity of *fcc* (200) diffraction peak. More significantly, at the pressure of 7.0(1) GPa, the *fcc* (111) reflection seems to have been replaced by the reflections of (100), (002) and (101) of the *hcp* phase, which appear on both sides of the ISF peak simultaneously. This strongly suggests that ISF is formed mainly within the (111) stackings and at the applied pressure of $\sim 7.0(1)$ GPa its population reaches a critical value, such that some ISF clusters overlaps with each other and triggers the structural phase transition to the *hcp* phase. This ISF-triggered *fcc*-to-*hcp* transformation is rather sluggish, persisting all way up to 19.4(2) GPa (the highest pressure applied in this study), which is one of the symbolic feature features characterizing HEAs. Lastly, although it may sound like the martensitic *fcc*-to-*hcp* transformation reported by Zhang et al. [2] and Tracy et al. [3], wherein the transformations were also very sluggish and persisted up to even higher pressures, the behavior had been attributed to different underlying reasons [2,3].

Based on the thermodynamics arguments, the transition pressure (P_{tr}) should be close or equal to the onset pressure. Thus, in the present case, the onset transition pressure of *fcc*-to-*hcp* phase for the quinary HEAs is recognized as 7.0(1) GPa, comparing with the values of 14 and 22.1 GPa reported for similar CoCrFeMnNi HEAs by Tracy et al. [3] and Zhang et al. [2], respectively. In the present case, the phase transformation thus not only is triggered at a much smaller applied pressure but also appears to have very different origins (*vide infra*). The lattice parameters of the present bulk CoCeFeMnNi at 7.0(1) GPa are $a = 3.5514(3) \text{ \AA}$ and $V/Z = 11.197(5) \text{ \AA}^3$ ($Z = 4$) for the *fcc* phase and $a = 2.4993(2) \text{ \AA}$, $c = 4.0868(3) \text{ \AA}$, $c/a = 1.635(1)$ and $V/Z = 11.053(6) \text{ \AA}^3$ ($Z = 6$) for the *hcp* phase, respectively. The volume reduction accompanying the phase transformation from *fcc*-to-*hcp* is small ($\sim 1.3\%$), which is slightly larger than with a 0.6(4) and 0.9% reported by Tracy et al. [3] and Ma et al. [24], respectively. The unit cell axial parameter ratio, c/a ($\sim 1.635(1)$), is slightly larger than the value of 1.633 for an ideal *hcp* structure. The calculated theoretical densities are 8.314(1) and 8.422(1) $\text{g}\cdot\text{cm}^{-3}$ for *fcc* and *hcp* structures at 7.0(1) GPa, respectively, and both increase with pressure. It is noted that the theoretical density of *hcp* phase is slightly higher than that of the *fcc* phase under high pressure. The experimental total enthalpy change ($\Delta^0 H$) for the *fcc* to *hcp* phase transformation at 7.0(1) GPa is estimated as follows [25]: $\Delta^0 H \approx P_{tr}(-\Delta V_{tr}) = 7.0 \text{ GPa} \times 0.144 \text{ \AA}^3 \times 6.02 \times 10^{23}/\text{mole} = 606.82 \text{ J}\cdot\text{mol}^{-1}$. This enthalpy change should be enough for the internal energy change required for reconstructing the *fcc* phase into the *hcp* phase. Considering the small stacking fault energy ($\sim 21 \text{ mJ/m}^2$) for the quinary HEAs reported previously [26,27], it is reasonable to expect that the energy provided by the pressure work done should be adequate to activate the dislocation activities associated with the formation of ISFs [28].

Fig. 10(b) further depicts the evolution of the ISF peak for pressures beyond 7.1(1) GPa. It is evident that after the emergence of transformation, the intensity of *hcp* phase gradually increases with increasing pressure, while the intensity of the ISF peak starts to decrease simultaneously from its maximum value. Between 10.9(1) to 19.4(2) GPa, intensity of the ISF and *hcp* phase continues to change, and the (200) reflection of the *fcc* phase appears to revive, indicating that the ISF as well as the *hcp* and *fcc* phases can coexist over a wide range of pressures, namely from 7.0(1) to 19.4(2) GPa.

The coexistence of multiple phases over a wide pressure range in fact is an indication of severe lattice distortion. Nonetheless, as shown in Fig. 11(a), although the inter-planar spacing are substantially different

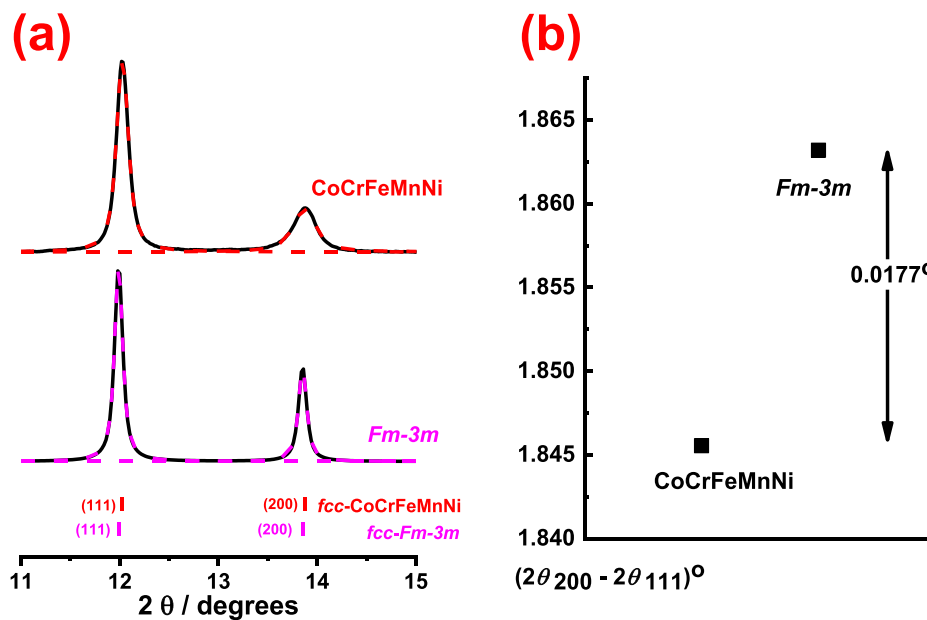


Fig. 8. (a) Representative ADXRD patterns of CoCrFeMnNi HEAs at ambient pressure. (b) Peak separations (111)–(200) for the CoCrFeMnNi HEAs and cubic $Fm\bar{3}m$ space group.

for the coexisting phases, its pressure-dependence up to 19.4(2) GPa is quite similar. Fig. 11(b) shows the pressure-dependence of the unit cell volume at the ambient temperature for the *fcc* phase of the quinary HEAs. The dotted line in Fig. 11(b) is the fit to the third-order BM equation of state for the *fcc* phase of the quinary HEAs. The obtained values of the zero-pressure isothermal bulk moduli (B_0) and its first derivative with respect to pressure (B'_0) for the *fcc* phase are 170(4) GPa and 4(1), respectively. The obtained B_0 value is larger than the value of 150(3) GPa reported by Tracy et al. [3] and 150.2 ± 4.6 GPa by Zhang et al. [2], respectively. The deviations may have been originated from the fact that all the samples were prepared differently. As mentioned above, since the intensity of any *hkl* reflection is directly proportional to the concentration or the volume fraction of the corresponding phase component [29], we track the phase evolution of the system in a more quantitative manner by intensity analyses. Peak areas are much more reliable than peak heights as a measure of intensity [30,31]. Fig. 11(c) shows the weight fraction (Wt. Frac.) of peak areas as a function of pressure for both *fcc* and *hcp* phases along with that of the ISF over the entire pressure range. The results displayed in Fig. 11(b) clearly reveal an intimate correlation connecting the appearance and diminution of the two phases and ISF of interest. As discussed above, the appearance of *hcp* phase starts at 7.0(1) GPa, where most of the *fcc* phase contains maximum amount of ISF. Subsequently, the weight fraction of *hcp* phase grows continuously with increasing pressure at the expense of the ISF regions in a rather sluggish manner, while the residual *fcc* phase remains essentially as a constant background. This strongly implies that the existence of ISF is indispensable for the forming of *hcp* phase in the present quinary HEAs under pressure. This observation is unprecedented and in contrast to the mechanism proposed by Tracy et al. [3], where the emergence of *hcp* phase at 14 GPa was specifically attributed to pressure-induced suppression of local magnetic moments in the original *fcc* phase. In fact, Zhang et al. [2] pointed out that the *hcp* structure could be obtained locally from an *fcc* structure by introducing stacking faults. However, we note that in their study no direct evidence of stacking faults was reported and, more intriguingly, the phase transition onset pressure was at 22.1 GPa, which is more than 3 times larger than that observed in the present study.

To sum up the phenomena observed, the proposed scenario suggests

that the microscale structural transition stems from the distorted *fcc* lattice resulting from the composition variations in the solidification cellular structures. The *fcc* structure then transforms to *hcp* structure under pressure via the outspreading of intrinsic stacking faults. The more quantitative details are briefly described as follows. When P is below 1.7(1) GPa, the *fcc* lattice undergoes elastic compressive deformation. Beyond that the lattice can no longer accommodate the elastic strain energy and plastic deformation arises due to dislocation gliding on the highest packed (111) planes, which, in turn, induces the formation of ISF, presumably owing to the small stacking fault energy inherent in this HEA system. When P increases to 4.6(1) GPa, the concentration of ISF continues to increase, whereas that of *fcc* region decreases, indicating that the dislocation glide mode still operates. As P was further increased to 7.0(1) GPa, the peak area of ISF increases continuously and eventually reaches a maximum value, wherein the areal extension of regions containing ISFs in the *fcc* matrix leads to mutual stacking of adjacent ISFs and results in the formation of the *hcp* phase. As P further increases to 19.4(2) GPa, the volume fraction of *hcp* phase reaches to about 93%, and that of the *fcc* phase decreases to less than 5% with trace amount of ISF remains in the background.

The evolutions of lattice parameters (a, c) of the *hcp* phase as a function of pressure are presented in Fig. 12(a). The linear compressibility along the *c*-axis $K_c = -(1/c)(dc/dP)_T = 1.982 \times 10^{-3}$ GPa $^{-1}$ is nearly two times larger than that along the *a*-axis $K_a = 1.081 \times 10^{-3}$ GPa $^{-1}$, indicating that the spacing between (001) planes is more susceptible to compression than that along the (100) planes. This is also manifested in the *c/a* ratio of the *hcp* phase of quinary HEAs as a function of pressure plotted in Fig. 12(b). The relationship between the *c/a* ratio and P can be fitted by a quadratic polynomial function with: $c/a = 1.638(1) + 0.0002(1)P - 6.0 \times 10^{-5}(1)P^2$. Refinement shows that this ratio is initially slightly larger than the value for ideal *hcp* phase, presumably due to the highly defective nature when it was first transformed from the ISF-containing *fcc* phase. Fig. 12(c) shows the unit cell volume as a function of the applied pressure for the *hcp* phase of the quinary HEAs. The dot line in Fig. 12(c) is the fitting result using the third-order BM equation of state for the *hcp* phase of the quinary HEAs. The obtained values of the zero-pressure isothermal bulk modulus (B_0) and its first derivative with respect to pressure (B'_0) for *hcp* phase of the quinary

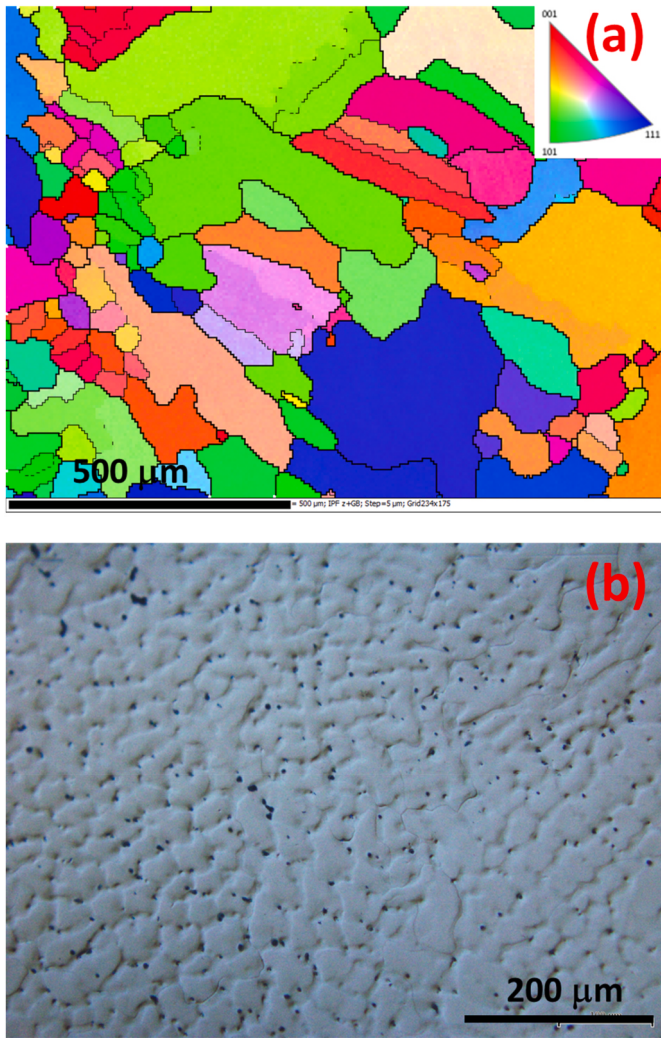


Fig. 9. (a) SEM EBSD IPF image and (b) OM image of microstructure of CoCrFeMnNi HEAs alloy.

HEAs are 188(2) GPa and 4(1), respectively. The value of bulk modulus is considerably larger than the values of 141(8) and 150.2 ± 4.6 GPa reported by Tracy et al. [3] and by Zhang et al. [2], respectively. It is noted that in [2,3] the reported bulk moduli of fcc phase were also larger than the transformed hcp phase, which opposite to what has been observed in the present case. Although it is suggestive that the hcp phase formed via the aids of ISF may be robust to the P than that formed via different routes, the underlying mechanisms, however, are calling for further studies. Finally, it is noted that the pressure effects and the associated phase transformations over the entire pressure range described above were only observed in the quinary HEAs but not in quaternary HEAs. This fact indicates the prominent role played by the manganese addition in giving rise to sluggish fcc-to-hcp phase transformation by introducing ISFs, which evidently lowered the kinetic barrier of fcc-to-hcp phase transformation suggested by Zhang et al. [2].

3.4.2. Results from the collimated focusing system

In order to double check that the observations presented above are not due to the local inhomogeneities, which can easily occur in concentrated solid solutions like the HEAs and might possibly pick up by the small X-ray beam size used in the Kirkpatrick-Baez (KB) focusing system at APS, we repeated the detailed pressure-dependent *in-situ* ADXRD measurements by using the collimated focusing X-ray at NSRRC, Taiwan. The beam size is about 150 μm in diameter, which is much

larger than the 26 μm × 28 μm beam size used in the KB system. Representative results are displayed in Fig. 13 with P up to 12.7(1) GPa. It is immediately noted that Fig. 13 essentially reproduces all the prominent features of Fig. 10 described above, except that, due to the larger incident beam size, the pattern becomes very spotty and the resolution of the hcp diffraction peaks is significantly blurred. Firstly, a discernible ISF peak manifested as a shoulder adjacent to the right-hand side of the (111) diffraction peak (the green dotted circle in Fig. 13) starts to emerge at 1.5(1) GPa, which is consistent with 1.7(1) GPa shown in Fig. 10(a). Secondly, the evolution of this ISF peak with pressure basically follows what was described above in Fig. 10. Namely, its intensity reaches a maximum around 6.5(1) GPa accompanied by the appearance of peaks corresponding to the hcp phase and gradually diminishing of the intensity of peaks corresponding to the fcc phase. Thirdly, it is also evident that the ISF as well as the hcp and fcc phases coexist over a pressure range of 6.5(1) to 12.7(1) GPa. Moreover, upon releasing the applied pressure back to ambient pressure, the position of all diffraction peaks shifts back to lower angles, presumably due to the decompression-induced volumetric expansion of all coexisting phases. These results not only lend further supports to our conjectures on the pressure-induced phase transformation discussed above, but also indicate the transition is irreversible because all the identified phases at high pressures preserved after decompressing. The lattice parameters under decompressed condition are: $a = 3.5899(72)$ Å and $V/Z = 11.5661(697)$ Å³ ($Z = 4$) for the fcc phase; $a = 2.5277(1)$ Å, $c = 4.1292(2)$ Å, $c/a = 1.633(1)$ and $V/Z = 11.423(2)$ Å³ ($Z = 6$) for the hcp phase. Comparing with $a = 3.5907(43)$ Å and $V/Z = 11.574(42)$ Å³ ($Z = 4$) for the pristine fcc phase at ambient, it is apparent that the decompressed fcc phase is still under substantial compressive strain. In contrast, the decompressed hcp phase appears to be in more relaxed state as compared to when it was first formed at around 7 GPa, wherein $a = 2.4993(2)$ Å, $c = 4.0868(3)$ Å, and $c/a = 1.633(1)$. In any case, the repeated ADXRD measurements confirm that the results reported here are genuine and the X-ray beam size does not affect the features of the diffraction pattern much, except that the original pattern becomes spotty and reduces the resolution of hcp diffraction peaks.

3.5. The structural and magnetic behavior of CoCrFeMnNi HEAs under pressure by NPD

As the last piece of the complementary evidence, Fig. 14 shows the NPD spectra of the quinary HEAs collected as a function of the applied pressure up to 8.9(2) GPa. It is evident that, for the pressure below 1.6 (1) GPa, there is no NPD peak corresponding to either the ISF or magnetic ordering phases. The lattice constant derived from these NPD data based on the fcc structure is 3.575(1) Å. The discernible new diffraction peak of ISF observed in the ADXRD pattern (at about 12.3°) is completely absent in the NPD pattern. The reason for the seemingly inconsistent results between the two patterns (Figs. 10 and 14) is mainly due to the fact that the scattering factors of X-ray and neutron for each element are different. The X-ray scattering factor (f) is simply proportional to the atomic number, thus, $f_{\text{Ni}} > f_{\text{Co}} > f_{\text{Fe}} > f_{\text{Mn}} > f_{\text{Cr}}$. However, the neutron scattering length (b) for manganese is negative and that for chromium, cobalt, iron, and nickel are positive, namely $b_{\text{Ni}} > b_{\text{Fe}} > b_{\text{Cr}} > b_{\text{Co}} > 0 > b_{\text{Mn}}$. As a result, the peak heights in the two powder-diffraction patterns are very different. Usually, the complex nature of the structure factors and the directional character of reciprocal space are both lost in NPD measurements. Consequently, the complementary analysis of X-ray and neutron powder patterns has been remaining as one of the most basic problems in identifying the structure of the ISFs.

As increasing the pressure up to 7.2(1) GPa, new diffraction peaks corresponding to the (100), (002), and (101)-reflections of the hcp structure start to emerge and become discernible on the right-hand side of the fcc (111) diffraction peak, as indicated in the inset (right panel) of Fig. 14. Notice that in Fig. 14, the reflections corresponding to WC and Pb are also displayed for comparison. Moreover, although the intensity

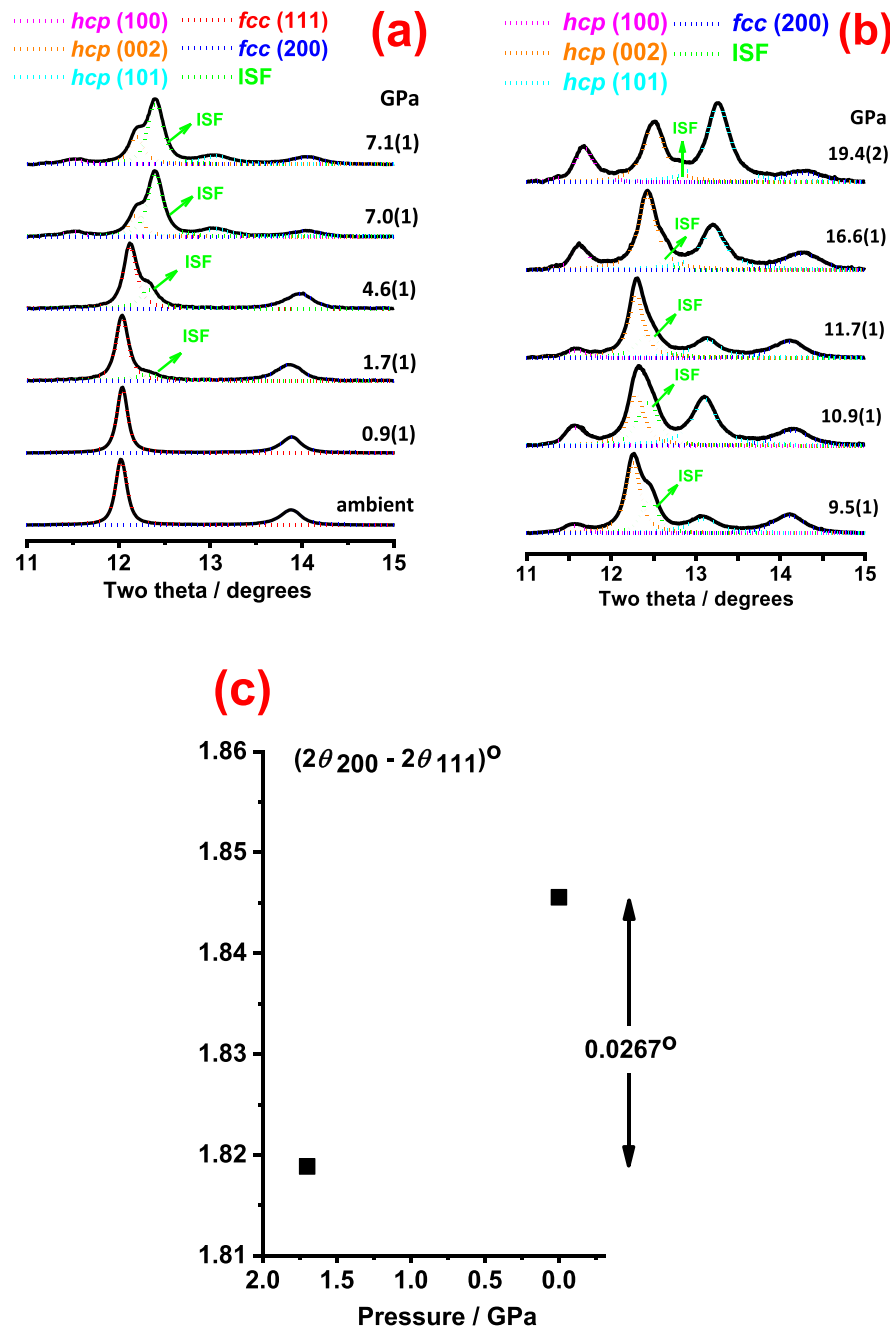


Fig. 10. Representative ADXRD patterns of CoCrFeMnNi at (a) ambient to 7.1(1) GPa (b) 9.5(1) to 19.4(2) GPa, by the KB focused X-ray beam. (c) Peak separations $2\theta_{200} - 2\theta_{111}$ for the CoCrFeMnNi HEAs at ambient conditions and 1.7(1) GPa.

of the new *hcp* peaks raises substantially with increasing pressure up to 8.9(2) GPa, the diffraction peaks from the initial *fcc* structure still remain visible (left panel, inset of Fig. 14). The coexistence of the *fcc* and *hcp* phases confirms that the phase transition is sluggish, which is consistent with the ADXRD results. Also, the onset pressure of *fcc* to *hcp* transition for the quinary HEAs determined by NPD measurement is about 7.2(1) GPa, which is very close to the value of 7.0(1) GPa obtained by ADXRD measurements.

It is noted that the peak intensity in NPD appears to be much weaker than that in ADXRD, presumably due to the much lower fluxes of neutron sources compared to the synchrotron X-ray sources. In addition, neutrons are scattered primarily by atomic nuclei. The nuclear dimensions of Co, Cr, Fe, Mn, and Ni, are roughly 100,000 times smaller

than the neutron wavelength ($\sim 1.5415 \text{ \AA}$), resulting in further reduction of the neutron scattering factors (scattering lengths or *b*'s). Consequently, in this study we didn't attempt to determine the lattice parameters of the *hcp* phase base on NPD data. Finally, the NPD results do not show evidence for the local magnetic moment suppression-induced destabilization of the initial *fcc* structure. Thus, although structural changes are found, it appears that the magnetic moment of each constituent element plays only a negligible role, if not none, in the pressure-induced phase transition behavior of the quinary HEAs. This is also consistent with the paramagnetic nature of the Cantor's alloy reported by Yu et al. [32], albeit that K. Jin et al. [33] did spot a possible anti-ferromagnetic or spin-glass transition at around 25 K in this quinary HEA.

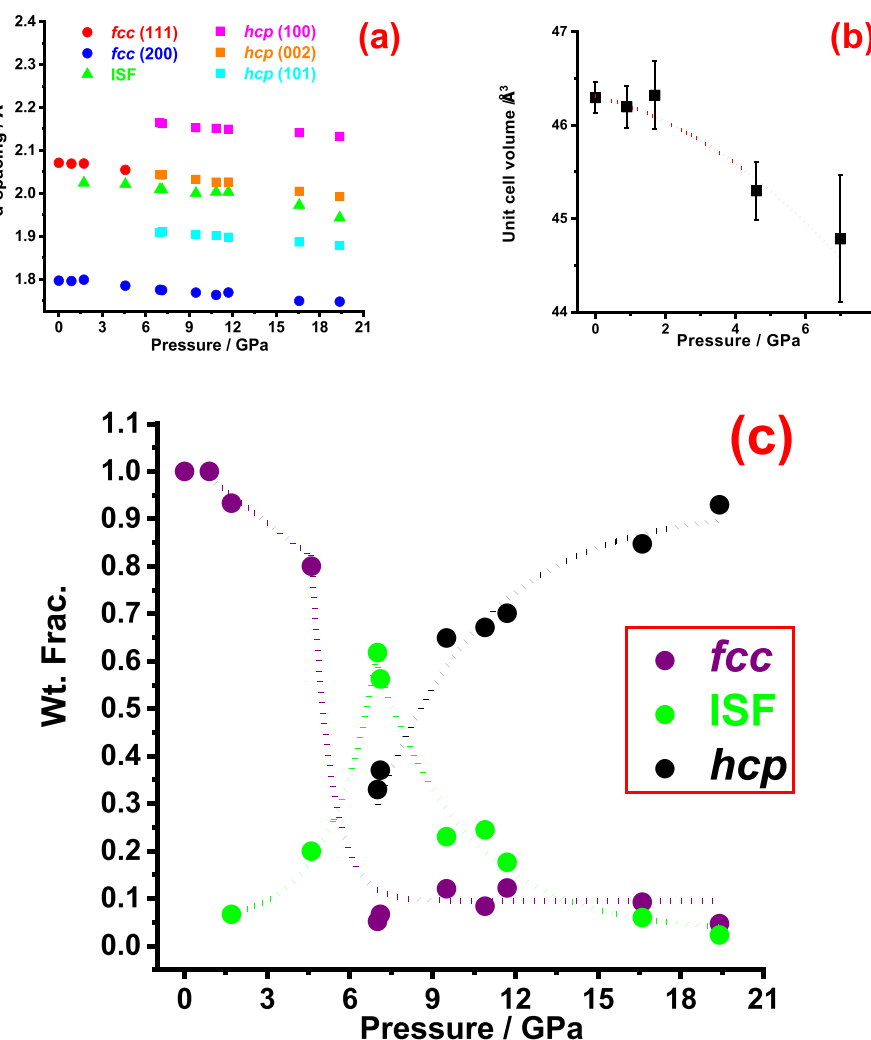


Fig. 11. (a) The variation of $d_{hkl}(\text{\AA})$ of CoCeFeMnNi with pressure (GPa) for the *fcc*, *hcp* phases and the intrinsic stacking fault. (b) Pressure dependence of the unit cell volume of *fcc* phase of CoCrFeMnNi at 300 K. The short dotted line illustrate the results of fitting of a third-order Birch-Murnaghan equation of state to the data corresponding to each phase. (c) Pressure dependence of the intensity weight fraction (Wt. Frac.) of *fcc*, *hcp* phases and the intrinsic stacking fault at 300 K in CoCrFeMnNi as purple, black, and green circles, respectively. (For interpretation of the references to colour in this figure legend, the reader is referred to the Web version of this article.)

4. Discussion

High configurational entropy is considered as the primary reason lending the single-phase stability exhibited in concentrated solid solution made of multi-principal elements, such as the HEAs. Nevertheless, pressure-induced structural phase transformation has been ubiquitously observed in HEAs [18–21], even though ADXRD evinces a pristine single-phase structure. In this study, we have shown that no pressure-induced phase transition was evidenced for the quaternary CoCrFeNi HEAs, even though the existence of ESF was clearly identified. On the other hand, for the quinary CoCrFeMnNi HEAs, pressure-induced *fcc*-to-*hcp* phase transition was observed and appears to be intimately correlated to the evolution of intrinsic stacking faults. To gain more insights in these intriguing observations, we try to give a more in-depth comparative discussion in the following.

According to Niu et al. [6] the shear displacements on successive $\{111\}$ planes in ternary CrCoNi can take three paths by virtue of gliding the Shockley partial dislocations on $\{111\}$ planes. For path 1, starting from the *fcc*, one-layer ISF, two-layer ESF, three-layer twins are generated by introducing Shockley partials with Burger vector, $b = \frac{1}{6}\langle 112 \rangle$, on adjacent $\{111\}$ planes. Further introduction of Shockley partials would lead to twin growth. For path 2, starting from the *fcc* structure, one-layer ISF is created by introducing a Shockley partial and the *hcp* stacking is obtained by skipping one plane and introducing the next partial on the second neighboring $\{111\}$ plane. The third path, on the

other hand, involves the sequence of forming one-layer ISF, two-layer ESF, three-layer twins, *hcp* structure and *hcp* growth. It is noted here that, although in Ref. [6] only the ternary CrCoNi was observed to exhibit the *fcc*-to-*hcp* after 55% of true tensile strain and the *hcp* phase was absent in parent quinary CoCrFeMnNi and other ternary derivatives due to the pronounced magnetic frustration of Mn, the proposed SF-facilitated *fcc*-to-*hcp* transformation paths appeared to be genuine for most cases. It's well known that the gliding of Shockley partial dislocations could disrupt the crystal lattice and result in a SF over the area on the glide plane swept by the gliding dislocation [30,31]. SF, by definition, represents a region where the close-packed atomic planes stack sequentially like ABCA/CABC, which has higher free energy than the original thermodynamically stable *fcc* lattice. Alternatively, CA/CA stacking could also be regarded as a four-layer *hcp* region embedded in the *fcc* lattice. Paths 2 and 3 indicated in [6] would both bring the closed-packed planes from an ABCABC type stacking in *fcc* to ABABAB stacking in *hcp* by virtue of forming an ISF first, which we believe might be relevant to the ISF facilitated *fcc*-to-*hcp* phase transition observed in the present study.

5. Conclusions

In-situ high-pressure ADXRD measurements have been systematically performed up to around 24.0(2) GPa to investigate the pressure-induced phase transitions in CoCrFeNi and CoCrMnFeNi HEAs. The results

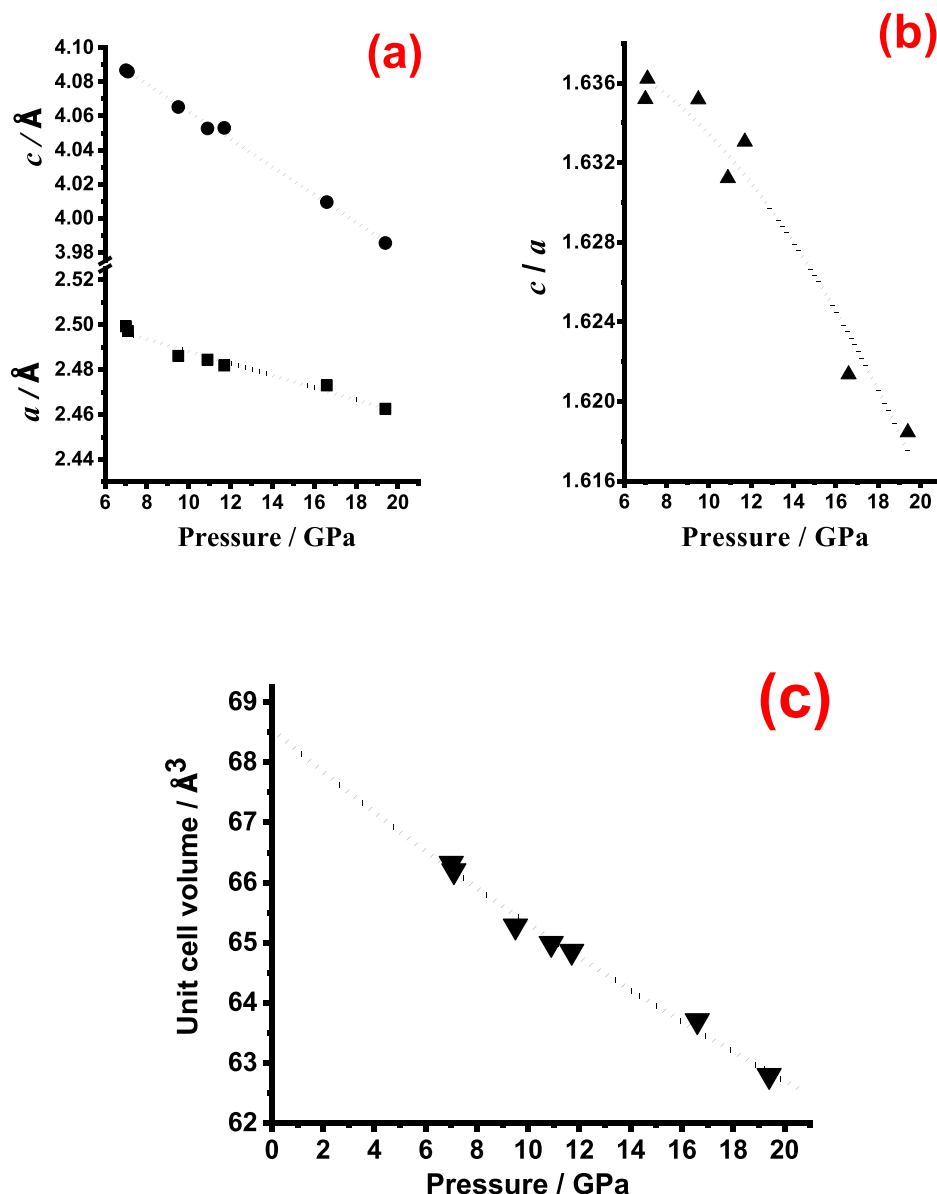


Fig. 12. (a) The change of *hcp* phase of CoCrFeMnNi cell parameters a , and c with increasing pressures. (b) The change of the unit cell axial ratio, c/a , with pressure. The dashed line is included by the quadratic polynomial fitting. (c) Pressure dependence of the unit cell volume of *hcp* phase of CoCrFeMnNi at 300 K. The dashed lines illustrate the results of fitting of a third-order Birch-Murnaghan equation of state to the data corresponding to each phase.

revealed no structural phase transition in the quaternary CoCrFeNi HEAs system up to the highest applied external pressure, despite that the extrinsic stacking faults were readily identified at ambient conditions. In contrast, for the quinary CoCrFeMnNi HEAs, both *in-situ* high-pressure ADXRD with two different beam sizes and NPD measurements revealed a sluggish *fcc*-to-*hcp* phase transformation with the aids of intrinsic stacking fault. The existence of the intrinsic stacking fault, at a relatively low pressure of 1.7(1) GPa, is experimentally delineated for the first time. The onset pressure for the *fcc*-to-*hcp* structural phase transition for the quinary CoCrFeMnNi HEAs is $\sim 7.0(1)$ GPa, which is about two to three times lower than those reported previously, indicating the prominent role played by lattice distortion effect introduced by manganese addition. Our results also suggested that, for CoCeFeMnNi HEAs, the sequence of pressure-induced phase-transformation can be described as follows: starting from the *fcc* structure, nucleation of one-layer intrinsic stacking fault at 1.7(1) GPa, formation of *hcp* structure

at around 7.0(1) GPa. The amount of *hcp* phase increases sluggishly with higher pressure and sustains over the entire pressure range studied. The present results apparently provide some new insights on the underlying mechanism of pressure-induced phase transition, which may also call for a more comprehensive theoretical and experimental study to fully delineate plastic deformation mechanism in CoCrFeMnNi HEAs.

CRediT authorship contribution statement

Chih-Ming Lin: prepared samples, performed synchrotron experiments, analyzed all synchrotron data, designed the research topic of this project. **Ching-Pao Wang:** performed synchrotron experiments. **Sean R. Shieh:** performed synchrotron experiments. **Yao-Jen Chang:** prepared samples, performed synchrotron experiments, analyzed all synchrotron data, analyzed all synchrotron data. **Tony Huang:** performed synchrotron experiments. **Dong-Zhou Zhang:** performed synchrotron

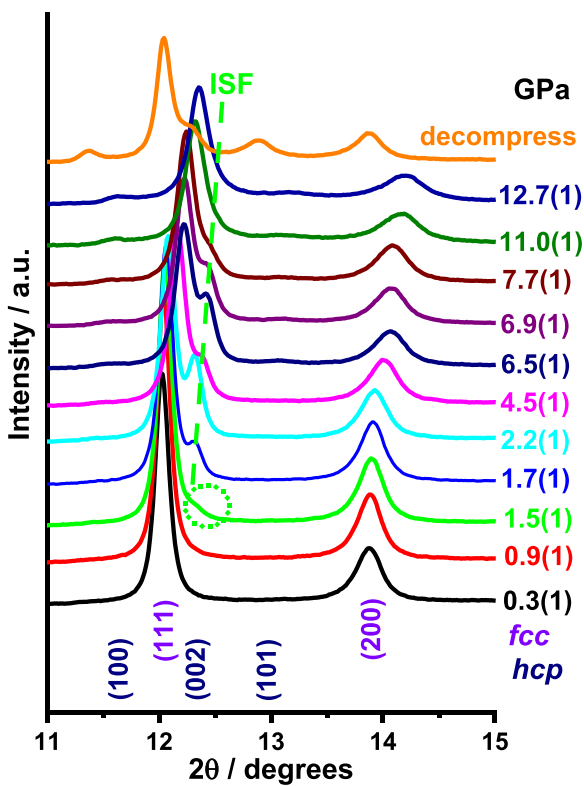


Fig. 13. Representative ADXRD patterns of CoCrFeMnNi at elevated pressures by using collimated X-ray with a beam size of ~ 150 mm in diameter.

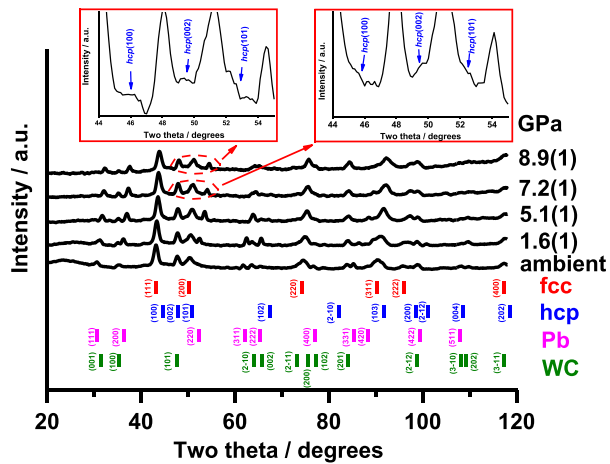


Fig. 14. Representative NPD patterns of CoCrFeMnNi up to 8.9(2) GPa.

experiments. **Chin-Wei Wang**: performed Neutron powder diffraction experiments. **An-Chou Yeh**: prepared samples. **Jenh-Yih Juang**: designed the research topic of this project.

Declaration of competing interest

The authors declare that they have no known competing financial interests or personal relationships that could have appeared to influence the work reported in this paper.

Acknowledgments

The authors are indebted to Prof. T. S. Chin and J. W. Yeh for their

critical comments on the manuscript. This work was financially supported by the "High Entropy Materials Center" from The Featured Areas Research Center Program within the framework of the Higher Education Sprout Project by the Ministry of Education (MOE) and from the Project MOST 109-2634-F-007-024- by Ministry of Science and Technology (MOST) in Taiwan. CML and his group members very much appreciate the beam time and help from the beamline 13-BM-C (Geo-SoilEnviroCARS) of Advanced Photon Source (APS) of Argonne National Laboratory (ANL) and the beamline BL01C2 at the National Synchrotron Radiation Research Center (NSRRC), Taiwan. CML and his group members very much appreciate the beam time and help from the high-intensity diffraction beamline (Wombat) at the Australian Nuclear Science and Technology Organisation (ANSTO). CML and JYJ are supported by MOST of Taiwan under grant #'s: 106-2112-M-009-013-MY3, 108-2112-M-007-020, 109-2112-M-007-025, and 109-2112-M-009-014-MY2.

References

- [1] F.X. Zhang, et al., Pressure-induced fcc to hcp phase transition in Ni-based high entropy solid solution alloys, *Appl. Phys. Lett.* 110 (2017), 011902, <https://doi.org/10.1063/1.4973627>.
 - [2] F. Zhang, et al., Polymorphism in a high-entropy alloy, *Nat. Commun.* 8 (2017) 15687, <https://doi.org/10.1038/ncomms15687>.
 - [3] C.L. Tracy, et al., High pressure synthesis of a hexagonal close-packed phase of the high-entropy alloy CrMnFeCoNi, *Nat. Commun.* 8 (2017) 15634, <https://doi.org/10.1038/ncomms15634>.
 - [4] V. Iota, J.H.P. Klepeis, C.S. Yoo, Electronic structure and magnetism in compressed 3d transition metals, *Appl. Phys. Lett.* 90 (2007), 042505, <https://doi.org/10.1063/1.2434184>.
 - [5] R. Torchio, O. Mathon, S. Pascarelli, XAS and XMCD spectroscopies to study matter at high pressure: probing the correlation between structure and magnetism in the 3d metals, *Coord. Chem. Rev.* 277 (2014) 80–94, <https://doi.org/10.1016/j.ccr.2014.02.024>.
 - [6] C. Niu, C.R. LaRosa, J. Miao, M.J. Mills, M. Ghazisaeidi, Magnetically-driven phase transformation strengthening in high entropy alloys, *Nat. Commun.* 9 (1) (2018) 1363, <https://doi.org/10.1038/s41467-018-03846-0>.
 - [7] J.C. Chervin, B. Canný, M. Mancinelli, Ruby-spheres as pressure gauge for optically transparent high pressure cells, *High Pres. Res.* 21 (2001) 305–314, <https://doi.org/10.1080/08957950108202589>.
 - [8] S. Klotz, J.C. Chervin, P. Munsch, G. L Marchand, Hydrostatic limits of 11 pressure transmitting media, *J. Phys. D Appl. Phys.* 42 (2009), 075413. [stacks.iop.org/JPhysD/42/075413](https://doi.org/10.1088/0022-3727/42/7/075413).
 - [9] Y. Meng, D.J. Weidner, Y. Fei, Deviatoric stress in a quasi-hydrostatic diamond anvil cell: effect on the volume-based pressure calibration, *Geophys. Res. Lett.* 20 (1993) 1147–1150, <https://doi.org/10.1029/93GL01400>.
 - [10] A.J. Studer, M.E. Hagen, T.J. Noakes, Wombat: the high-intensity powder diffractometer at the OPAL reactor, *Physica B* 385 (2006) 1013–1015, <https://doi.org/10.1016/j.physb.2006.05.323>.
 - [11] J. Rodríguez-Caravajal, Recent advances in magnetic structure determination by neutron powder diffraction, *Physica B* 192 (1993) 55–69, [https://doi.org/10.1016/0921-4526\(93\)90108-1](https://doi.org/10.1016/0921-4526(93)90108-1).
 - [12] U. Dahlborg, et al., Structure of some CoCrFeNi and CoCrFeNiPd multicomponent HEA alloys by diffraction techniques, *J. Alloys Compd.* 681 (2016) 330–341, <https://doi.org/10.1016/j.jallcom.2016.04.248>.
 - [13] L. Balogh, G. Ribárik, T. Ungárák, Stacking faults and twin boundaries in fcc crystals determined by x-ray diffraction profile analysis, *J. Appl. Phys.* 100 (2006), 023512, <https://doi.org/10.1063/1.2216195>.
 - [14] Y. Wang, et al., Probing deformation mechanisms of a FeCoCrNi high-entropy alloy at 293 and 77 K using in situ neutron diffraction, *Acta Mater.* 154 (2018) 79–89, <https://doi.org/10.1016/j.actamat.2018.05.013>.
 - [15] B.E. Warren, E.P. Warekois, Measurements of stacking faults in cold-worked alpha Brass, *J. Appl. Phys.* 24 (1953) 951–952, <https://doi.org/10.1063/1.1721408>.
 - [16] B.E. Warren, *X-Ray Diffraction*, Dover Publications, Inc., 1990 equation (13.68).
 - [17] L.E. Copeland, R.H. Bragg, Quantitative X-ray diffraction analysis, *Anal. Chem.* 30 (2) (1958) 196–201.
 - [18] P.F. Fewster, A new theory for X-ray diffraction, *Acta Crystallogr. A* 70 (2014) 257–282, <https://doi.org/10.1107/S05327331400117X>.
 - [19] C. Lazo, S. Heinze, First-principles study of magnetic exchange force microscopy with ferromagnetic and antiferromagnetic tips, *Phys. Rev. B* 84 (2011) 144428, <https://doi.org/10.1103/PhysRevB.84.144428>.
 - [20] C. Kittel, *Introduction to Solid State Physics*, seventh ed., John Wiley & Sons, Inc., 1996. Table, 7.
 - [21] J.C. Jamieson, The phase behavior of simple compounds, *Phys. Earth Planet. In.* 3 (1970) 201–203.
 - [22] S.M.C. van Bohemen, The nonlinear lattice expansion of iron alloys in the range 100–1600 K, *Scripta Mater.* 69 (2013) 315–318, <https://doi.org/10.1016/j.scriptamat.2013.05.009>.
 - [23] G. Laplanche, P. Gadaud, O. Horst, F. Otto, G. Eggeler, E.P. George, Temperature dependencies of the elastic moduli and thermal expansion coefficient of an

- equiatomic, single-phase CoCrFeMnNi high-entropy alloy, *J. Alloys Compd.* 623 (2015) 348–353, <https://doi.org/10.1016/j.jallcom.2014.11.061>.
- [24] D. Ma, B. Grabowski, F. Körmann, J. Neugebauer, D. Raabe, Ab initio thermodynamics of the CoCrFeMnNi high entropy alloy: importance of entropy contributions beyond the configurational one, *Acta Mater.* 100 (2015) 90–97, <https://doi.org/10.1016/j.actamat.2015.08.050>.
- [25] T.S. Duffy, Y. Wang, Reviews in Mineralogy Vol. 37, in: R.J. Hemley (Ed.), *Ultrahigh-Pressure Mineralogy: Physics and Chemistry of the Earth's Deep Interior*, Mineralogical Society of America, Washington, DC, 1998, pp. 425–457.
- [26] A.J. Zaddah, C. Niu, C.C. Koch, D.L. Irving, Mechanical properties and stacking fault energies of NiFeCrCoMn high-entropy alloy, *JOM* 65 (2013) 1780–1789.
- [27] S. Huang, W. Li, S. Lu, F. Tian, J. Shen, E. Holmström, L. Vitos, Temperature dependent stacking fault energy of FeCrCoNiMn high entropy alloy, *Scripta Mater.* 108 (2015) 44–47.
- [28] R. Smallman, D. Green, The dependence of rolling texture on stacking fault energy, *Acta Mater.* 12 (1964) 145–154.
- [29] L.E. Copeland, R.H. Bragg, Quantitative X-ray diffraction analysis, *Anal. Chem.* 30 (2) (1958) 196–201.
- [30] J. Ruska, L.I. Gauckler, J. Lorenz, H.U. Rexer, The quantitative calculation of SiC polytypes from measurements of X-ray diffraction peak intensities, *J. Mater. Sci.* 14 (1979) 2013–2017.
- [31] F.R. Feret, Determination of the crystallinity of calcined and graphitic cokes by X-ray diffraction, *Analyst* 123 (1998) 595–600, <https://doi.org/10.1039/A707845E>. April.
- [32] P.F. Yu, et al., The high-entropy alloys with high hardness and soft magnetic property prepared by mechanical alloying and high-pressure sintering, *Intermetallics* 70 (2016) 82–87, <https://doi.org/10.1016/j.intermet.2015.11.005>.
- [33] K. Jin, et al., Tailoring the physical properties of Ni-based single-phase equiatomic alloys by modifying the chemical complexity, *Sci. Rep.* 6 (2016) 20159, <https://doi.org/10.1038/srep20159>.